**Rare Metal Materials and Engineering**
Volume 55, Issue 10, October 2026
Available online at www.rmme.ac.cn

Science Press

**Cite this article as**: Bao Mengting, Guo Ke, Jiang Yun, et al. Arc-Erosion Behavior and Mechanism of Ag/ZnO/$La_2Sn_2O_7$ Composites in $N_2$, $CO_2$ and Their Mixtures with c-$C_4F_8$[J]. Rare Metal Materials and Engineering, 2026, 55(10): 2450-2462. DOI: https://doi.org/10.12442/j.issn.1002-185X.20250462.

ARTICLE

# Arc-Erosion Behavior and Mechanism of Ag/ZnO/$La_2Sn_2O_7$ Composites in $N_2$, $CO_2$ and Their Mixtures with c-$C_4F_8$

**Bao Mengting, Guo Ke, Jiang Yun, Wang Bingtang, Liu Zhuhan, Feng Yi**

*School of Materials Science and Engineering, Hefei University of Technology, Hefei 230009, China*

**Abstract:** $La_2Sn_2O_7$ powder was synthesized via chemical co-precipitation, and the Ag/ZnO/$La_2Sn_2O_7$ composites were prepared by hot-pressed sintering. The arc-erosion behavior and mechanisms of the composites were investigated at a constant voltage of 7 kV in $CO_2$, $N_2$, $CO_2$/c-$C_4F_8$, and $N_2$/c-$C_4F_8$ mixtures. The results show that the difference in arc breakdown current is very small across different atmospheres, while the erosion area, arc energy, and arc duration in mixed gas are clearly smaller than those in $CO_2$ and $N_2$. As the content of c-$C_4F_8$ rises, the breakdown strength in mixed gas increases gradually and is higher than that in $CO_2$ and $N_2$. The optical images of the arc show that the arc volume in mixed gas is obviously smaller than that in single-gas $CO_2$ or $N_2$, and the arc volume decreases gradually with the increase in c-$C_4F_8$ content. The erosion morphology analysis indicates that more pores, spattered particles, and cracks are present in the composites after arc-erosion in $CO_2$ and $N_2$. In the gas mixture, the erosion area is the smallest in the $N_2$/c-$C_4F_8$ (80/20) mixture, and particles and pores are significantly reduced. The low arc energy observed in $N_2$/c-$C_4F_8$ mixtures significantly reduces arc volume and erosion area. X-ray photoelectron spectroscopy results reveal partial decomposition of $La_2Sn_2O_7$ into $La_2O_3$ and $SnO_2$, while AgF and $CF_x$ compounds are identified on eroded surfaces in c-$C_4F_8$ containing mixtures.

**Key words:** Ag/ZnO/$La_2Sn_2O_7$ composites; protective atmosphere; arc-erosion behavior; erosion mechanism

## 1 Introduction

High-voltage switches serve as pivotal nodes in power grids and depend critically on electrical contacts. The properties of these contact materials consequently govern device reliability and operational lifetime[1]. These contacts require high electrical conductivity, stable contact resistance, exceptional resistance to arc-erosion, and superior thermal conductivity[2-3]. Ag-based composites are composed of a silver matrix and discrete reinforcements. They address inherent limitations of conventional alloys, such as high-temperature microstructural instability and property trade-offs. Typically, oxides, carbides, or borides serve as reinforcing phases, thereby enhancing arc-erosion resistance and mitigating mass loss[4-5]. Ag/CdO stands out among Ag/MeO composites for its superior electrical contact properties, including excellent anti-welding and anti-erosion capabilities, as well as high thermal and electrical conductivity[6]. Despite the outstanding performance of Ag/CdO, the toxicity of cadmium and its compounds severely restricts its use[7]. ZnO is a non-toxic, eco-friendly, low-cost material with a wide bandgap and excellent properties for various optoelectronic applications[8-10]. Ag/ZnO, characterized by low contact resistance, low cost, and eco-friendliness, is a leading candidate to replace Ag/CdO[11-12]. Guzmán et al[13] demonstrated that zinc exhibits physical and chemical properties analogous to cadmium, while numerous switch performance studies indicated the superiority of Ag/ZnO over other silver metal oxides under resistive loads. However, Ag/ZnO exhibits relatively weak interfacial bonding. During discharge, ZnO tends to aggregate at the contact surface, compromising material stability and degrading electrical contact performance[14].

Rare metals are characterized by their low crustal abundance and dispersed occurrence[15]. Recent advances underscore the promise of rare-earth oxides. In particular, lanthanum (La) exhibits the highest chemical activity among rare-earth elements, inferior only to alkali and alkaline-earth metals, and readily reacts with impurities in electrical contact

Received date: October 09, 2025
Foundation item: National Natural Science Foundation of China (51871085)
Corresponding author: Feng Yi, Ph. D., Professor, School of Materials Science and Engineering, Hefei University of Technology, Hefei 230009, P. R. China, E-mail: fyhfut@163.com

materials to form oxides[16]. Rare-earth oxides will accumulate on the surface of composites because of the action of arcing, stabilizing the arc duration, and improving the arc-erosion resistance of the contacts[17]. Zhang et al[18] demonstrated that $La_2Sn_2O_7$ increased molten pool viscosity and improved Ag/$SnO_2$ wettability. Cao et al[19] reported its efficacy in enhancing the comprehensive performance of Ag/$SnO_2$ composites.

Protective atmospheres also offer a critical approach to enhancing arc-quenching performance in high-voltage equipment. Currently, $SF_6$ circuit breakers with sulfur hexafluoride ($SF_6$) as the insulating medium dominate in the high-voltage grid, super grid, and ultra-high-voltage grid[20]. However, $SF_6$ is a potent greenhouse gas, with a global warming potential (GWP) of 23 900 relative to $CO_2$ and a lifetime of up to 3200 years in the atmosphere, thereby driving severe climate impacts[21]. Consequently, developing eco-friendly alternatives to $SF_6$ is imperative. Zhao et al[22] reported an ascending breakdown strength ($O_2$<air<$CO_2$<$N_2$<Ar<$SF_6$) and an inverse correlation with arc energy. While $CO_2$ and $N_2$ are used commercially as insulating/switching media, their inferior dielectric strength and current-interruption capacity relative to $SF_6$ necessitate larger equipment, potentially offsetting the replacement benefits[23]. Alternative gases like c-$C_4F_8$ exhibit promise, demonstrating breakdown strength 1.2–1.4 times larger than that of $SF_6$, high electronegativity, and lower GWP (1/3 of that of $SF_6$) [24]. Nevertheless, its high liquefaction temperature and cost preclude direct application. Liu et al[25] reported comparable arc-quenching performance for $SF_6$ and c-$C_4F_8$, surpassing that of air. Zhang et al[26] further analyzed c-$C_4F_8$/$N_2$/$CO_2$ mixtures using the steady-state Thomson method.

In this study, the arc-erosion resistance properties and mechanism of Ag/ZnO/$La_2Sn_2O_7$ composites in different atmospheres under load voltage of 7 kV were studied, and the arc-erosion behavior of Ag/ZnO/$La_2Sn_2O_7$ composites in $CO_2$, $N_2$, and mixed gases with different ratios of c-$C_4F_8$ was investigated. By comparing arc-erosion parameters, the improvement in arc-extinguishing performance upon addition of c-$C_4F_8$ for $CO_2$ and $N_2$ buffer gases was studied, and the composition of the erosion region was investigated.

## 2 Experiment

### 2.1 Preparation of Ag/ZnO/$La_2Sn_2O_7$ composites

$La_2Sn_2O_7$ nanopowder was prepared by chemical co-precipitation. $La(NO_3)_3·6H_2O$ and $SnCl_4·5H_2O$ were used as raw materials, and $NH_3·H_2O$ was used as precipitant. The raw materials were weighed and dissolved in deionized water. The precipitant was added slowly to the mixed solution during stirring. When the pH of the mixed solution reached 10–11, the precipitant was stopped, and the mixture was stirred for 1 h. After stirring, the precipitate was washed sequentially with deionized water and absolute ethanol by centrifugation, then dried and ground into powder. Finally, the powder was calcined at 1100 °C for 1 h in a muffle furnace (KSL-1700X-S) to obtain $La_2Sn_2O_7$ nanopowder.

Silver powder (<40 μm), ZnO powder (3–5 μm), and the prepared $La_2Sn_2O_7$ powder were mixed at a mass ratio of 90: 8: 2, mechanically mixed for 4 h, and then sintered in a vacuum hot-pressing furnace (ZT-40-20Y). Argon was chosen as a protective atmosphere. The temperature was raised to 600 ℃ and held for 30 min, then heated to 800 ℃ at 10 ℃/min, and finally to 850 ℃ at 10 ℃/1.5 min. The temperature was maintained at 850 ℃ for 60 min, and then the furnace was cooled to room temperature. The pressure was maintained at 30 MPa throughout the process. The Ag/ZnO/$La_2Sn_2O_7$ composite was cut into several strip-shaped test blocks measuring 32 mm×5 mm×3 mm for electrical resistivity testing and square test blocks measuring 10 mm×10 mm×3 mm for other tests. The test blocks were polished with sandpaper until the surfaces were free of scratches.

### 2.2 Arc-erosion test

As depicted in Fig. 1, the sample serves as the cathode on a horizontal moving platform, opposite to a stationary tungsten rod anode. The sealed chamber was first evacuated and then filled with the desired gas mixture to 0.1 MPa. This evacuation-filling cycle was repeated three times to ensure gas purity. The description of the mixed gas environments is presented in Table 1. A constant voltage of 7 kV was applied between the electrodes. The moving platform then advanced the cathode toward the anode at a uniform speed until electrical breakdown occurred. The current-time and voltage-time curves were recorded with an oscilloscope (UTD2102 CEX). The arc-erosion process was recorded with a high-speed camera (FASTCAM Nova S16).

### 2.3 Characterization methods

In this experiment, Archimedes' method of immersion was

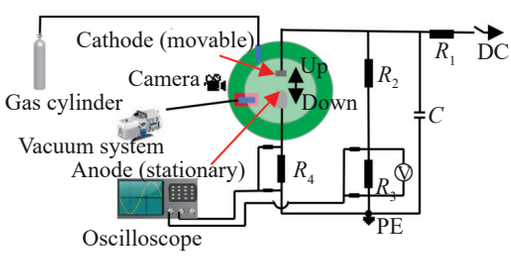


Fig.1 Schematic diagram of the experimental device

**Table 1 Description of the mixed gas environment(%)**

| Atmosphere | C-C-90-10 | C-C-80-20 | C-C-70-30 | N-C-90-10 | N-C-80-20 | N-C-70-30 |
|---|---|---|---|---|---|---|
| Concentration of $CO_2$ | 90 | 80 | 70 | - | - | - |
| Concentration of $N_2$ | - | - | - | 90 | 80 | 70 |
| Concentration of c-$C_4F_8$ | 10 | 20 | 30 | 10 | 20 | 30 |

used to measure the density of the samples. The electrical resistivity of the samples was measured using the double-arm bridge method. A Brinell hardness tester (HBV-30A) was used to measure the hardness of the samples. A quenched steel ball with a diameter of 1 mm was selected as the indenter, with a load of 10 kg and a holding time of 30 s. The composite's thermal diffusivity was measured by laser flash analysis in a laser thermal conductivity meter (LFA457). To reduce errors, the results were averaged from three repeated tests. The phase composition of the Ag/ZnO/$La_2Sn_2O_7$ composites was characterized by the X-ray diffractometer (XRD, X-pert PRO MPD). Focused ion beam (FIB, Crossbeam 350) and high-resolution transmission electron microscope (HRTEM, Talos F200X G2) were used to observe the microstructure of Ag/ZnO/$La_2Sn_2O_7$ composites. The surface morphology of $La_2Sn_2O_7$ powder and composite samples before and after arc-erosion was observed by scanning electron microscope (SEM, Gemini500), field emission transmission electron microscope (TEM, JEM-2100F), and 3-dimensional laser confocal scanning microscope (3DLSCM, VK-X250). The chemical composition of the arc-eroded composite surface was determined by X-ray photoelectron spectroscopy (XPS, ESCALAB250) and energy-dispersive X-ray spectroscopy (EDS, UltimMax100).

## 3 Results and Discussion

### 3.1 Characterization of $La_2Sn_2O_7$ nanopowders and composites

Fig. 2a is a TEM image of the $La_2Sn_2O_7$ nanopowder. The $La_2Sn_2O_7$ nanopowder has uniform particle sizes ranging from 50 nm to 100 nm. The powder belongs to the cubic crystal system, with polyhedral crystal grains. Fig. 2b is XRD pattern of the $La_2Sn_2O_7$ nanopowder, showing no impurity peaks, indicating that the prepared $La_2Sn_2O_7$ nanopowder has high purity.

Fig. 3 shows the phase composition and microstructure of Ag/ZnO/$La_2Sn_2O_7$ composites. Uniform dispersion of ZnO and $La_2Sn_2O_7$ in the Ag matrix is evident in Fig. 3a, while XRD analysis in Fig. 3b reveals only diffraction peaks corresponding to Ag, ZnO, and $La_2Sn_2O_7$, indicating that no chemical reaction occurs during synthesis.

To further elucidate the interfacial bonding conditions within the material, Ag/ZnO/$La_2Sn_2O_7$ composites were characterized by HRTEM. By analyzing the lattice fringes in HRTEM images, the crystal plane spacing is determined. Fig. 4a shows that the lattice spacing of 0.203 nm corresponds to the (200) plane of Ag, 0.281 nm corresponds to the (100) plane of ZnO, and 0.162 nm corresponds to the (622) plane of $La_2Sn_2O_7$. From Fig. 4b–4g, it can be observed that there are obvious interfaces between various phases in Ag/ZnO/$La_2Sn_2O_7$ composites. EDS line scanning results in Fig. 4h – 4j reveal that there are obvious compositional gradient characteristics at the interfaces between the phases in Ag/ZnO/$La_2Sn_2O_7$ composites, and the transition layers between each phase are only 20 – 30 nm thick. The corresponding crystal plane spacings shown in Fig. 4a and the results in Fig. 4h–4j indicate that Ag, ZnO, and $La_2Sn_2O_7$ in the composites form strong mechanical bonds with each other. An appropriate interface combination is crucial to the properties of Ag/ZnO/

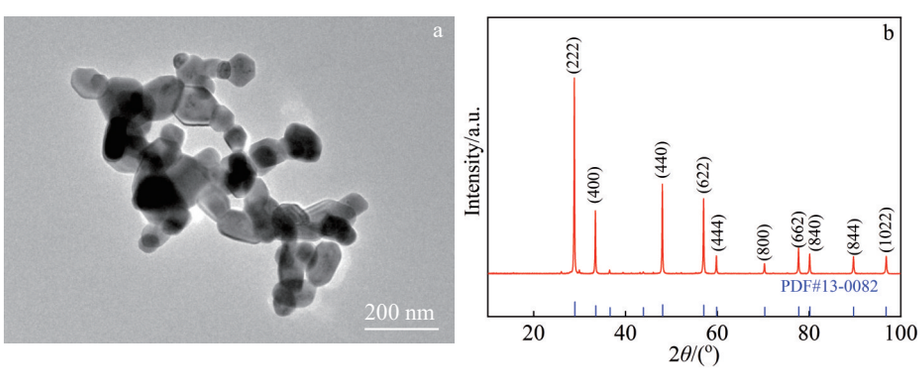


Fig.2 TEM image (a) and XRD pattern (b) of $La_2Sn_2O_7$ nanopowder

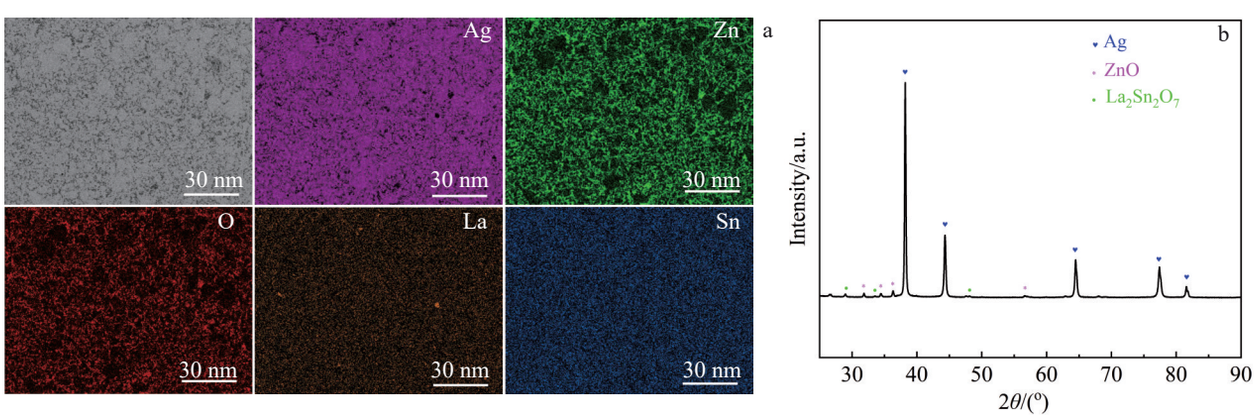


Fig.3 SEM image (a) and XRD pattern (b) of Ag/ZnO/$La_2Sn_2O_7$ composites

$La_2Sn_2O_7$ composites.

For electrical contact materials, good electrical and thermal conductivities are essential, and higher hardness is also very important in actual work. The physical properties of Ag/ZnO/$La_2Sn_2O_7$ composites are shown in Table 2.

### 3.2 Arc-erosion characteristics

To characterize the arc optical topography, high-speed images were acquired at 220 000 frames/s in $N_2$, $CO_2$, and specific gas mixtures (Fig. 5). Table 3 summarizes the resulting arc-erosion parameters for Ag/ZnO/$La_2Sn_2O_7$ composites at 7 kV across these atmospheres, with all values representing averages from three replicate experiments. Obviously, the breakdown current shows minimal variation. Breakdown strength, a key indicator of a material's arc-erosion resistance, quantifies the difficulty of arc initiation: higher values indicate greater resistance to electrical discharge. The breakdown strength is calculated according to Eq.(1)[27]:

$$E = \frac{U}{d} \tag{1}$$

where $E$ represents the breakdown strength (kV/cm); $U$ represents the load voltage (kV); $d$ represents the discharge distance (cm). In Table 3, the breakdown strength of the composite material increases with increasing c-$C_4F_8$ concentration, and the composite material's breakdown strength in the mixed gas containing c-$C_4F_8$ is much higher than that in $CO_2$ or $N_2$. The breakdown strength of the composite material in the C-C-70-30 and N-C-70-30 mixed gases is 203% and 240% of the breakdown strength of the composites in $CO_2$ and $N_2$, respectively. This is because c-$C_4F_8$ is a highly electronegative, ultra-high-voltage dielectric with excellent arc-extinguishing performance.

In addition, arc energy is also an important indicator of the arc-erosion resistance of composites. The lower the arc energy, the lower the degree of erosion. In Fig.5, in the single-gas atmospheres, the arc is larger and brighter in $CO_2$ than in $N_2$. In the same buffer gas, higher c-$C_4F_8$ concentrations reduce arc volume and intensity, indicating lower arc energy. Notably, in both single-gas and mixed-gas configurations, arcs in $N_2$-based gases are consistently smaller and less intense than those in $CO_2$-based counterparts, reflecting greater energy release with $CO_2$ as the buffer gas. The arc energy is

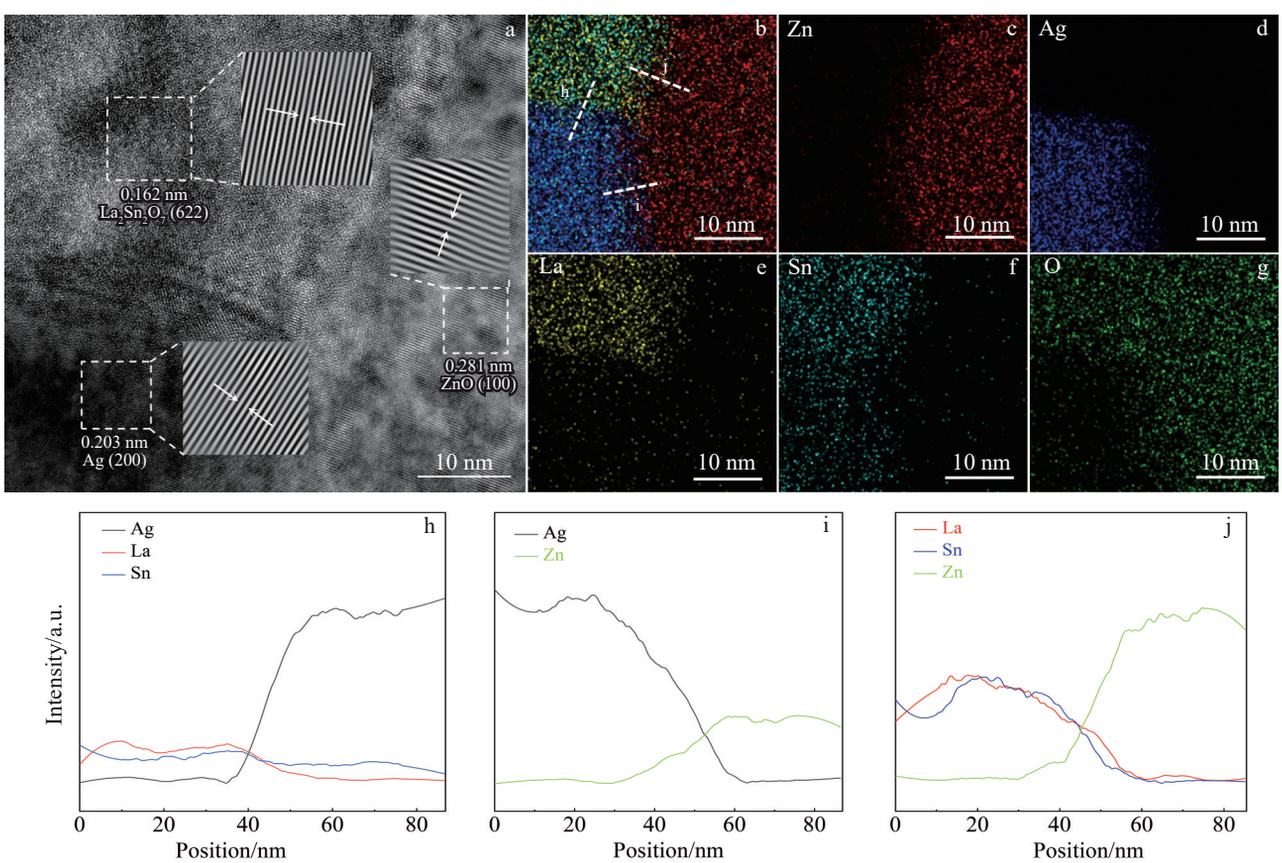


Fig.4 HRTEM image of the grain boundary region (a) and corresponding EDS elemental mappings (b–g); EDS line scanning results along dotted lines marked in Fig.4b (h–j)

**Table 2 Physical properties of Ag/ZnO/$La_2Sn_2O_7$ composites**

| Density/g·cm$^{-3}$ | Electrical resistivity/×10$^{-8}$ Ω·m | Brinell hardness/HB | Thermal diffusivity/×10$^{-6}$ m$^2$·s$^{-1}$ |
|---|---|---|---|
| 9.4920 | 2.471 | 77.75 | 104.196 |

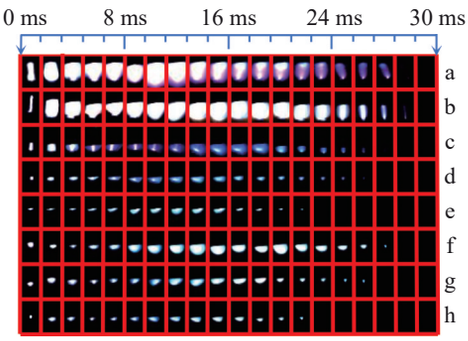


Fig.5 Optical images of arc discharges in different atmospheres: (a) $N_2$; (b) $CO_2$; (c) N-C-90-10; (d) N-C-80-20; (e) N-C-70-30; (f) C-C-90-10; (g) C-C-80-20; (h) C-C-70-30

calculated by Eq.(2)[28]:

$$W = UIt \tag{2}$$

where $W$ represents arc energy (J); $U$ represents load voltage (kV); $I$ represents breakdown current (A); $t$ represents arc duration (ms). Corresponding to the values of breakdown current and arc duration in Table 3, it can be calculated that the arc energy under different atmospheres is: $CO_2$>$N_2$>C-C-90-10>N-C-90-10>C-C-80-20>N-C-80-20>C-C-70-30>N-C-70-30, which is consistent with the arc variation trends in Fig.5.

Generally, the anode region receives electron flow from the arc column, serving as the electron transfer path to the cathode region. An arc column is composed of plasma, in which electrons, ions, atoms, and molecules have different masses, and mutual collisions maintain the arc. The key to maintaining continuous arc discharge lies in thermal equilibrium, and plasma temperature is critical to this equilibrium. Liu et al[29] established Eq. (3) for the relative deviation between electron and gas temperatures, based on the premise that an electron's energy gain rate from an electric field balances its collisional loss rate. This formula explains the mechanism of thermal equilibrium.

$$\frac{T_e - T_g}{T_e} = \frac{3\pi m_z \left(\lambda_e eE\right)^2}{32 m_e \left(\frac{3}{2} KT_e\right)^2} \tag{3}$$

where $m_z$ represents the mass of heavy particles, $m_e$ represents the mass of electrons, $T_e$ represents the electron temperature, $T_g$ represents the gas temperature, $\lambda_e$ represents the mean free path of electrons, $E$ represents the electric field strength, $e$ represents the electron charge, and $K$ is the Boltzmann constant. A smaller difference between $T_e$ and $T_g$ facilitates the maintenance of local thermal equilibrium. The molecular masses of the buffer gases c-$C_4F_8$, $CO_2$, and $N_2$ used in this experiment are 200, 44, and 37, respectively. Thus, the value of $m_z$ in the formula is $N_2$< $CO_2$< N-C-90-10< C-C-90-10 < N-C-80-20< C-C-80-20< N-C-70-30< C-C-70-30. C-C-70-30 has the largest $m_z$ and therefore the largest $T_e$–$T_g$ value, making it difficult to maintain thermal equilibrium and resulting in shorter arc durations for the C-C-70-30 mixture, consistent with the trend in Table 3.

### 3.3 Macroscopic morphology of Ag/ZnO/$La_2Sn_2O_7$ composite after arc-erosion in different atmospheres

The eroded surface morphologies of composites in different atmospheres are shown in Fig. 6. Significant differences in surface morphologies after arc-erosion are observed in these atmospheres, and the arc-erosion region can be divided into a severely eroded central region and a slightly eroded edge region in each atmosphere. Fig. 6a – 6h reveal distinct morphological differences in the eroded areas. Under $N_2$ and $CO_2$ atmospheres, erosion manifests as elongated strips, whereas in C-C and N-C mixed gases, it exhibits relatively regular, predominantly elliptical shapes. Table 4 shows that the largest eroded area occurs in $CO_2$, followed by that in $N_2$. Furthermore, within mixed gases of the same composition, the eroded area is larger in C-C than in N-C atmospheres, reaching as low as 0.882 $mm^2$ in the N-C-80-20 mixture. The corresponding 3-dimensional (3D) morphologies of the composites are shown in Fig. $6a_1$ – $6h_1$, where colors indicate height, concave areas are marked in green and blue, and protruding areas are marked in red.

When an arc is generated, the temperature is extremely high, often exceeding 6500 K, well above the melting point of Ag[30]. Molten Ag droplets are splashed under great thrust, and protrusions and pits are produced after solidification. From Table 4, it can be seen that when a mixed gas is used as the buffer gas, the protrusion height generally increases with increasing c-$C_4F_8$ concentration, which is related to the gas's thermal conductivity. In mixtures with high thermal conductivity, rapid arc discharge reduces surface heat accumulation and accelerates the solidification of splashed silver droplets, thereby increasing bump height. Consistent with this mechanism, the heat transfer coefficients in different atmospheres follow the order: c-$C_4F_8$>$N_2$>$CO_2$[31]. However, the heights of the $CO_2$ and $N_2$ bumps are higher than those in the mixed gas with c-$C_4F_8$ because the arc energy in the mixed gas is lower and its effect on the material is smaller.

### 3.4 Microstructure of Ag/ZnO/$La_2Sn_2O_7$ composite after arc-erosion in different atmospheres

The microstructure and composition of Ag/ZnO/$La_2Sn_2O_7$ composite after arc-erosion in $CO_2$ and $N_2$ gases are shown in Fig. 7. The microstructures of Ag/ZnO/$La_2Sn_2O_7$ composites

**Table 3 Arc-erosion parameters of Ag/ZnO/$La_2Sn_2O_7$ composites in different atmospheres**

| Atmosphere | $CO_2$ | C-C-90-10 | C-C-80-20 | C-C-70-30 | $N_2$ | N-C-90-10 | N-C-80-20 | N-C-70-30 |
|---|---|---|---|---|---|---|---|---|
| Breakdown current/A | 29.6 | 29.6 | 29.6 | 29.4 | 29.4 | 29.2 | 29.2 | 29.2 |
| Arc duration/ms | 27.7 | 26.2 | 25.6 | 23.6 | 27.8 | 26.4 | 25.8 | 23.7 |
| Breakdown strength/kV·$cm^{-1}$ | 22.37 | 28.20 | 42.59 | 45.47 | 20.70 | 30.67 | 46.71 | 49.73 |

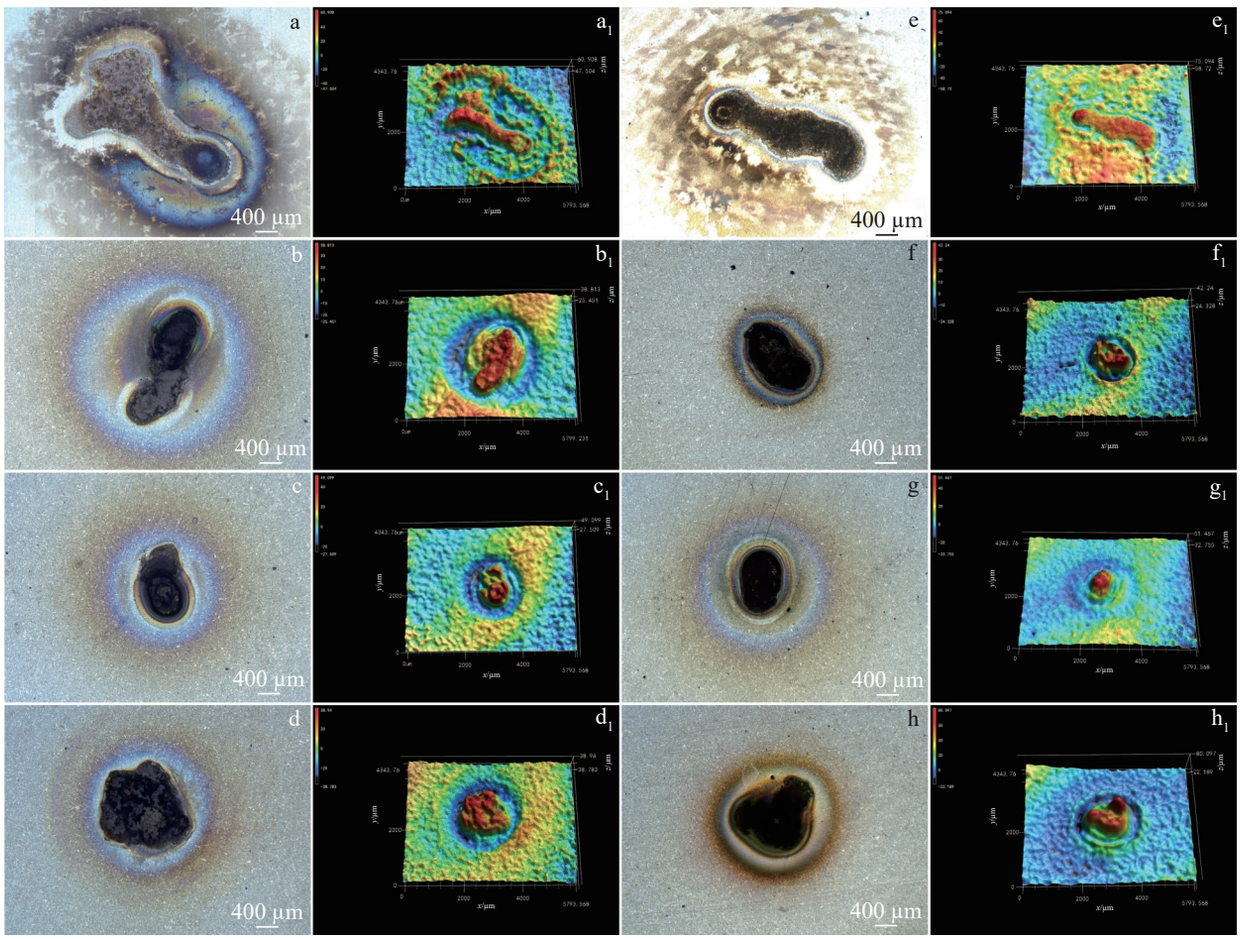


Fig.6 Optical images (a–h) and corresponding 3D laser confocal scanning results ($a_1$–$h_1$) of eroded composites' surface appearances in different atmospheres: (a, $a_1$) $CO_2$; (b, $b_1$) C-C-90-10; (c, $c_1$) C-C-80-20; (d, $d_1$) C-C-70-30; (e, $e_1$) $N_2$; (f, $f_1$) N-C-90-10; (g, $g_1$) N-C-80-20; (h, $h_1$) N-C-70-30

**Table 4 Erosion area and undulation height of Ag/ZnO/$La_2Sn_2O_7$ composites under different atmospheres**

| Atmosphere | $CO_2$ | C-C-90-10 | C-C-80-20 | C-C-70-30 | $N_2$ | N-C-90-10 | N-C-80-20 | N-C-70-30 |
|---|---|---|---|---|---|---|---|---|
| Erosion area/$mm^2$ | 3.295 | 1.690 | 1.262 | 2.180 | 2.345 | 1.330 | 0.882 | 1.652 |
| Undulate height/μm | 108.4 | 64.2 | 76.6 | 77.7 | 133.8 | 66.6 | 84.2 | 102.3 |

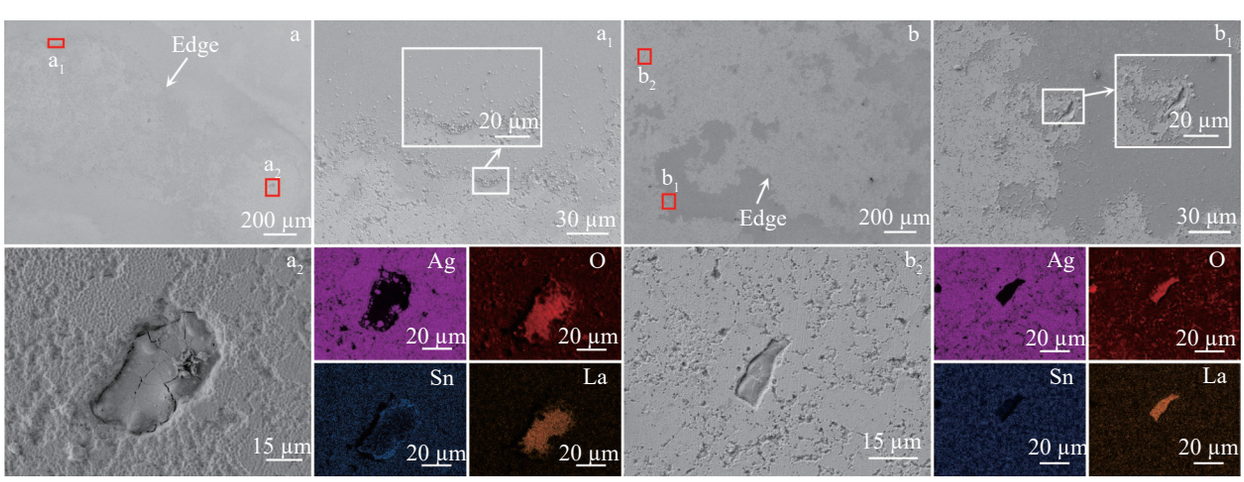


Fig.7 SEM and EDS mapping images of arc-erosion areas in $CO_2$ (a, $a_1$, $a_2$) and $N_2$ (b, $b_1$, $b_2$)

after arc-erosion in $CO_2$ are shown in Fig. 7a. Fig. 7$a_1$ is an enlarged view of the red box at the erosion edge. In Fig. 7$a_1$, many spattered particles and pores are present at the material's erosion edge, and the spattering range is relatively large. There are pores on the particle's surfaces. During arc discharge, $CO_2$ decomposes into $O_2$ and CO at high temperatures. Molten silver dissolves substantial $O_2$, which is subsequently released upon solidification as the temperature drops, promoting pore formation. Fig. 7$a_2$ is an enlarged view of the red box at the erosion center. EDS scanning at the crater of the erosion center in $CO_2$ shows that Sn, La, and O exist in the erosion zone, so the particle in Fig. 7$a_2$ is presumed to be $La_2O_3$, a decomposition product of $La_2Sn_2O_7$.

The microstructure of Ag/ZnO/$La_2Sn_2O_7$ composite after arc-erosion in $N_2$ is shown in Fig. 7b. Fig. 7$b_1$ is an enlarged view of the red box at the erosion edge. In Fig. 7$b_1$, a few spattered particles and obvious pits are observed at the erosion edge. The spattering range is smaller than that in $CO_2$ gas, and there are fewer surface pores. This phenomenon can be attributed to the lower arc energy in $N_2$ than in $CO_2$. Fig. 7$b_2$ is an enlarged view of the red box at the erosion center. The crater in the center is a typical erosion morphology. EDS results indicate that Sn, La, and O elements are present in this region. Similarly, the large particle in Fig. 7$b_2$ is mainly composed of La and O elements. It is speculated that the decomposition product of $La_2Sn_2O_7$ after arc-erosion of the composite in $N_2$ is also $La_2O_3$.

Fig. 8 shows the micromorphologies of Ag/ZnO/$La_2Sn_2O_7$ composite after arc-erosion in C-C gas mixture. Consistent with Table 4, Fig. 8 shows that the smallest erosion area occurs in the C-C-80-20 atmosphere. Within this gas mixture, pores and fine cracks are present at both the erosion edge and the center of the composite material. With increasing c-$C_4F_8$ content, traces of liquid flow and pores at the edge decrease, and the number of particles increases. Fig. 9a shows EDS mapping of the arc-erosion area in C-C-70-30, where C and F are detected. This suggests that $CF_x$ may form on the composite surface post-erosion. Such deposits align with prior studies, where higher c-$C_4F_8$ concentrations promote severe carbon deposition during discharge, and adherent carbon on spattered silver droplets can degrade electrical contact performance[32]. Notably, Fig. 8$a_2$ – 8$c_2$ reveal that C-C-80-20 mixtures exhibit the least arc-erosion.

The microstructure of Ag/ZnO/$La_2Sn_2O_7$ composite after arc-erosion in N-C mixed gas is shown in Fig. 10, in which the erosion area in N-C-80-20 mixture gas is obviously smaller than that in the other two mixture gases, which is also consistent with the parameters in Table 4. Compared with the C-C mixture gas, there are fewer pores in the eroded area than in the N-C mixture gas, but relatively more flocs are gathered around the eroded edge, and the silver body is exposed at the erosion center. Similarly, for the C-C mixture gas, with increasing c-$C_4F_8$ content, the traces of liquid flow at the edge decrease, and the number of particles increases. As shown in

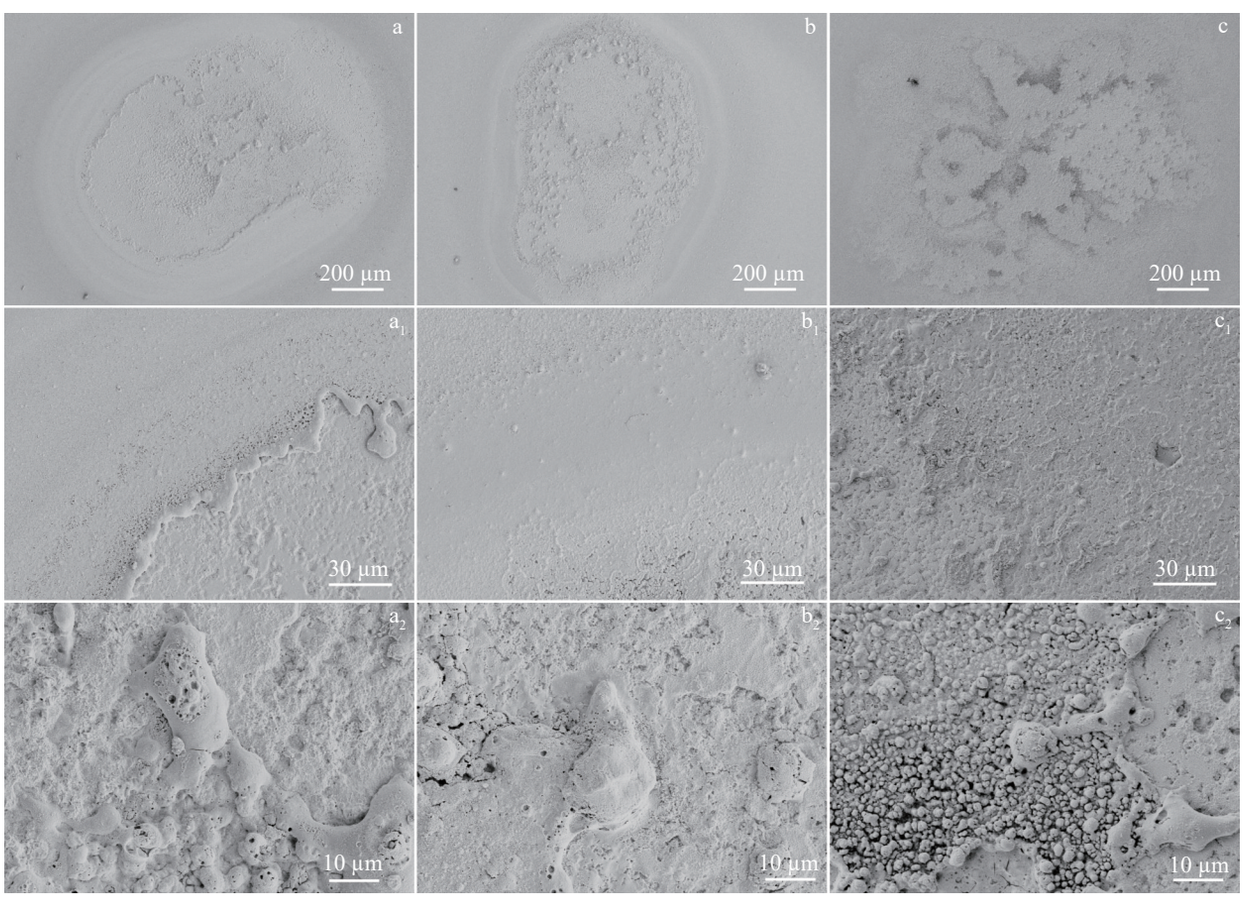


Fig.8 Micromorphologies of arc-erosion areas in different atmospheres: (a, $a_1$, $a_2$) C-C-90-10; (b, $b_1$, $b_2$) C-C-80-20; (c, $c_1$, $c_2$) C-C-70-30

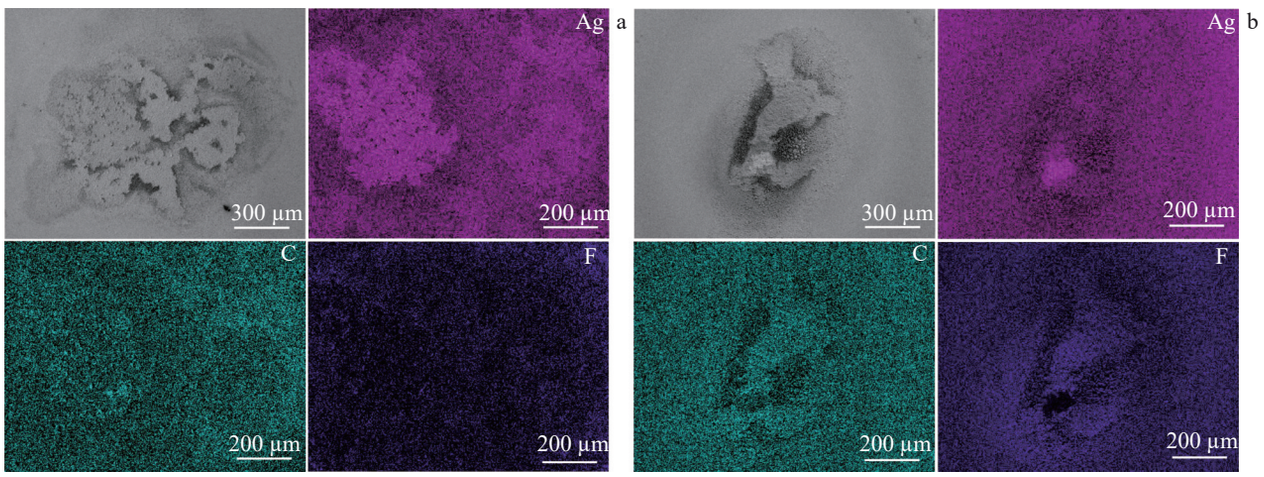


Fig.9 SEM images and EDS mapping images of arc-erosion area in different mixture gases: (a) C-C-70-30; (b) N-C-70-30

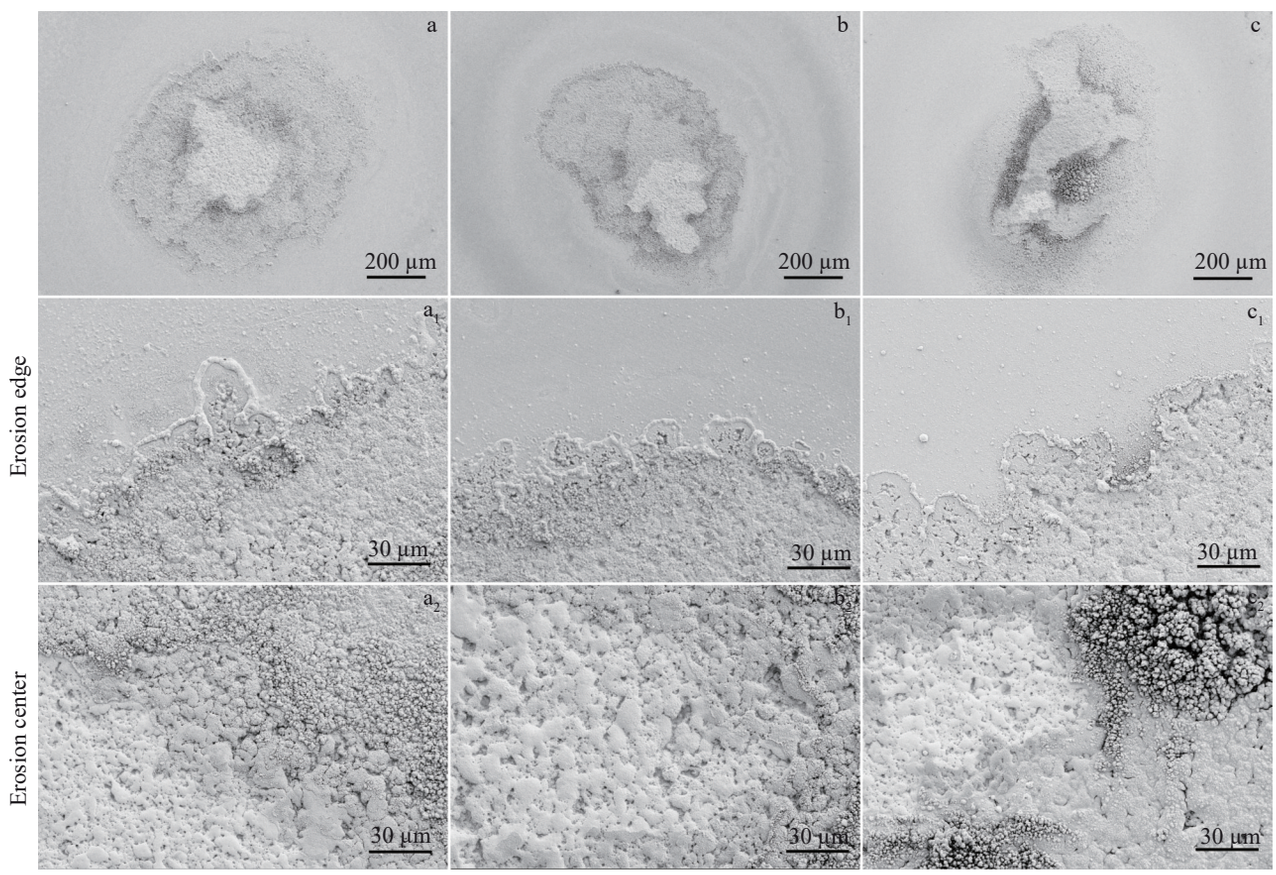


Fig.10 Micromorphologies of arc-erosion areas in different atmospheres: (a, $a_1$, $a_2$) N-C-90-10; (b, $b_1$, $b_2$) N-C-80-20; (c, $c_1$, $c_2$) N-C-70-30

Fig. 9b, the EDS mapping image of the arc-erosion area in N-C-70-30 shows that there is a silver-rich area in the erosion center, and C and F are detected in the erosion area, suggesting that $CF_x$ may also exist on the surface of the composite material after erosion. Also, due to carbon deposition from excessive c-$C_4F_8$, the erosion center in the N-C-70-30 mixed gas is relatively severely eroded. According to Fig. 10$a_1$ – 10$c_1$, the erosion is the least affected by arc-erosion in N-C-80-20 mixtures.

### 3.5 Arc-erosion mechanism

#### 3.5.1 Reaction products

To characterize arc-discharge reaction products, XPS was used to analyze the erosion region of Ag/ZnO/$La_2Sn_2O_7$ composites exposed to different buffer gases. Fig. 11 shows XPS analysis results of Ag/ZnO/$La_2Sn_2O_7$ composite after arc-erosion in $CO_2$. XPS results obtained by fitting the Ag 3d peak, Zn 2p peak, La 3d peak, and Sn 3d peak are shown in Fig. 11a–11d, respectively. The fitting results in Fig. 11a show

peaks at 373.98 and 368.03 eV, corresponding to the Ag $3d_{3/2}$ and Ag $3d_{5/2}$ peaks, which are characteristics of metallic silver and its oxidation products, respectively. The two peaks of Zn 2p are centered at about 1021.43 and 1044.53 eV, corresponding to the emission of Zn $2p_{3/2}$ and Zn $2p_{1/2}$ photoelectrons, respectively. These values are consistent with the $Zn^{2+}$ data in ZnO. In the La 3d spectra, the La $3d_{5/2}$ peak at 835.9 eV and the La $3d_{3/2}$ peak at 852.7 eV correspond to $La_2O_3$. In Fig. 11d, the Sn 3d peak also corresponds to the Sn $3d_{3/2}$ peak at 495.31 eV and the Sn $3d_{5/2}$ peak at 486.64 eV. This shows that $La_2Sn_2O_7$ partially decomposes into $La_2O_3$ and $SnO_2$ during arc-erosion of Ag/ZnO/$La_2Sn_2O_7$ composites in a $CO_2$ atmosphere. Analysis reveals that the reaction products in $CO_2$ are $Ag_2O$, $La_2O_3$, and $SnO_2$.

Fig. 12 shows XPS analysis results of Ag/ZnO/$La_2Sn_2O_7$ composite after arc-erosion in $N_2$. Ag $3d_{5/2}$ peak at 367.68 eV and Ag $3d_{3/2}$ peak at 373.68 eV correspond to Ag. Zn $2p_{1/2}$ peak at 1044.78 eV and Zn $2p_{3/2}$ peak at 1021.78 eV correspond to ZnO. XPS results of the fitted La 3d peak indicate that the La $3d_{3/2}$ peak with a binding energy of 852.48 eV and La $3d_{5/2}$ peak with a binding energy of 835.98 eV correspond to $La_2O_3$. In Fig. 12d, both the Sn $3d_{3/2}$ peak at 495.28 eV and the Sn $3d_{5/2}$ peak at 486.54 eV correspond to $SnO_2$. These observations indicate that $La_2Sn_2O_7$ partially decomposes during arc-erosion of Ag/ZnO/$La_2Sn_2O_7$ composites in $N_2$, forming $La_2O_3$ and $SnO_2$. This shows that the reaction products in $N_2$ are $La_2O_3$ and $SnO_2$.

The XPS spectra of the erosion area of the Ag/ZnO/$La_2Sn_2O_7$ composite in C-C mixed gas are shown in Fig. 13. In Fig. 13a, there are peaks at 373.98 and 368.13 eV, corresponding to the Ag $3d_{3/2}$ and Ag $3d_{5/2}$ peaks, respectively, which correspond to metallic silver and its oxidation products respectively. At elevated temperatures in C-C mixed gas, $CO_2$ decomposes into $O_2$ and CO; the resulting $O_2$ then reacts with Ag to form $Ag_2O$. Two peaks at 373.18 and 367.53 eV belong to the Ag-F bond of AgF. Zn $2p_{1/2}$ peak at 1045.02 eV and Zn $2p_{3/2}$ peak at 1022.08 eV correspond to ZnO. F 1s peaks are shown in Fig. 13c, which reveals peaks at 682.43, 684.48, and 688.38 eV, assigned to AgF, $LaF_3$, and $CF_x$, respectively. Notably, $CF_x$ serves as an ideal electrical insulator and thermal conductor, exhibiting excellent chemical stability that mitigates adverse effects from surface carbon deposition. The La 3d XPS spectrum of $LaF_3$ (Fig. 13d) is divided into La $3d_{5/2}$ and La $3d_{3/2}$, with a difference of 16.70 eV[33]. As a result, the reaction products in the C-C mixture gas are $Ag_2O$, AgF, $CF_x$, and $LaF_3$.

In Fig. 14a, the Ag $3d_{5/2}$ peak at 368.03 eV and the Ag $3d_{3/2}$ peak at 374.08 eV correspond to metallic Ag, and the peaks at 373.13 and 367.41 eV correspond to AgF. The lower intensity of the Ag 3d peak for AgF in N-C mixtures compared to C-C mixtures reflects the lower arc energy in N-C environments. The Zn $2p_{1/2}$ peak at 1044.9 eV and the Zn $2p_{3/2}$ peak at 1022.28 eV are characteristics of ZnO. Fig. 14c shows three F 1s peaks at 682.03, 684.53, and 688.03 eV, assigned to AgF, $LaF_3$, and $CF_x$, respectively. The intensity of the F 1s peak corresponding to AgF in the N-C mixture is lower than that in the C-C mixture, which is consistent with the above results. As in C-C, La 3d XPS spectrum of $LaF_3$ in Fig. 14d is divided into La $3d_{5/2}$ and La $3d_{3/2}$, and the difference is also 16.70 eV. Analysis indicates that the reaction products in the N-C mixture gas are AgF, $CF_x$, and $LaF_3$.

### 3.5.2 Reaction mechanism

The arc-erosion mechanism of Ag/ZnO/$La_2Sn_2O_7$ composites in different atmospheres is shown in Fig. 15.

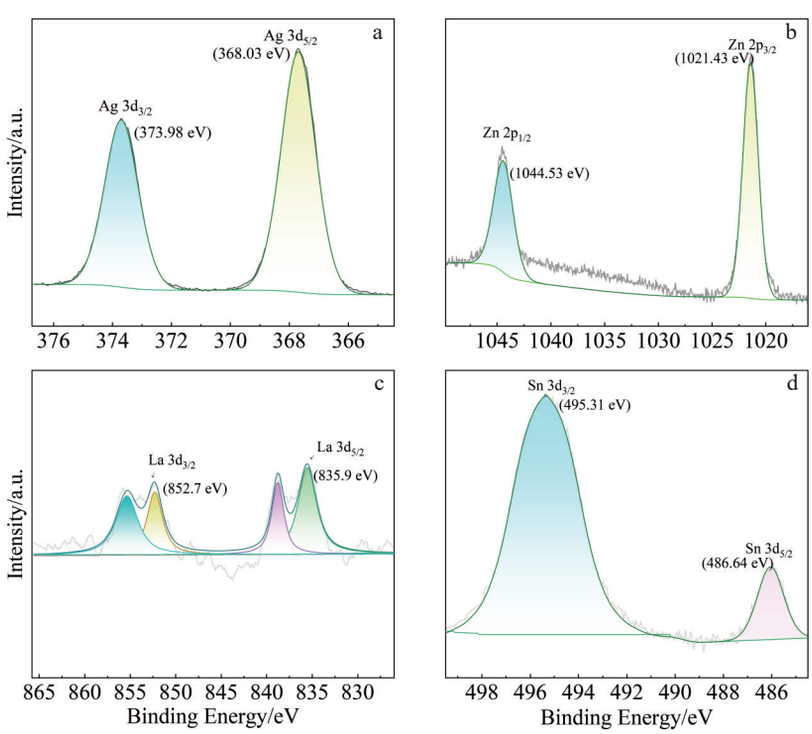


Fig.11 XPS spectra of erosion area of composites in $CO_2$: (a) Ag; (b) Zn; (c) La; (d) Sn

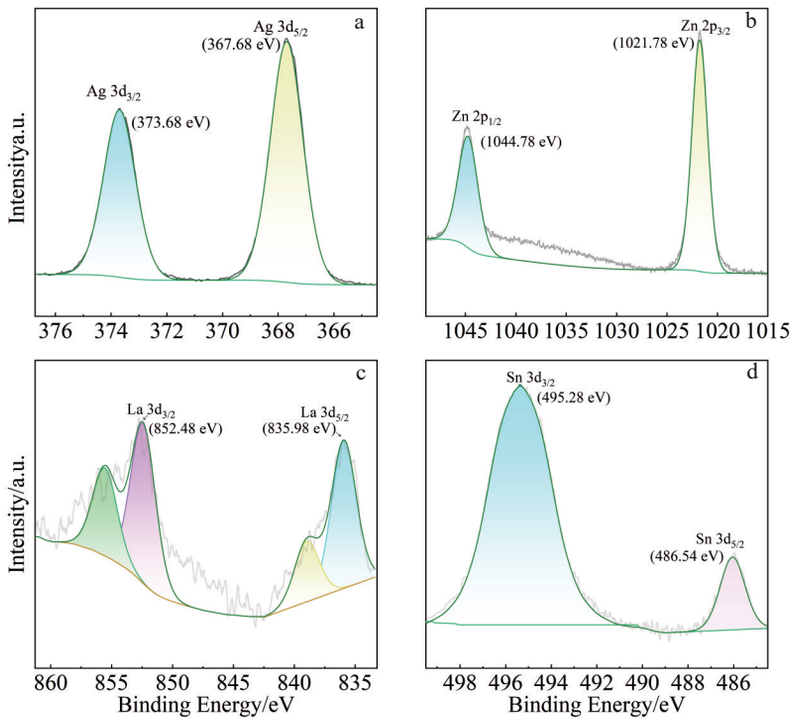


Fig.12 XPS spectra of the erosion area of composites in $N_2$: (a) Ag; (b) Zn; (c) La; (d) Sn

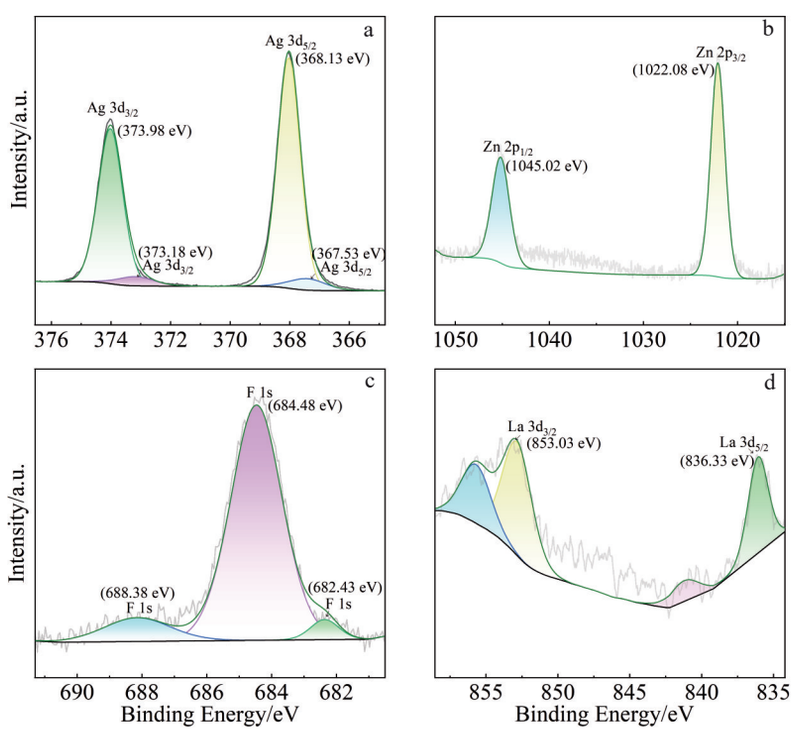


Fig.13 XPS spectra of the erosion area of composites in C-C mixed gas: (a) Ag 3d; (b) Zn 2p; (c) F 1s; (d) La 3d

During discharge, high-energy arc bombardment melts and evaporates the material, forming a molten pool at the erosion center. Subsequently, molten Ag droplets are sputtered from the surface under the synergistic effect of arc electromagnetic force and material vapor pressure. Ag in composites is affected by extremely high temperatures; silver vapor is generated in the cavity, and Ag is rich in vapor. $La_2Sn_2O_7$ is ionized into $La^{3+}$, $Sn^{4+}$, and $O^{2-}$, and this bond-breaking process requires a large amount of energy.

In a $CO_2$ atmosphere, $CO_2$ is ionized into CO and $O^{2-}$ at extremely high temperatures during arc discharge, and sufficient $O_2$ combines with $Ag^+$, $La^{3+}$, and $Sn^{4+}$ to form $Ag_2O$, $La_2O_3$, and $SnO_2$, respectively. Unlike in a $CO_2$ atmosphere, in an $N_2$ atmosphere, since $O^{2-}$ is not supplied from the outside,

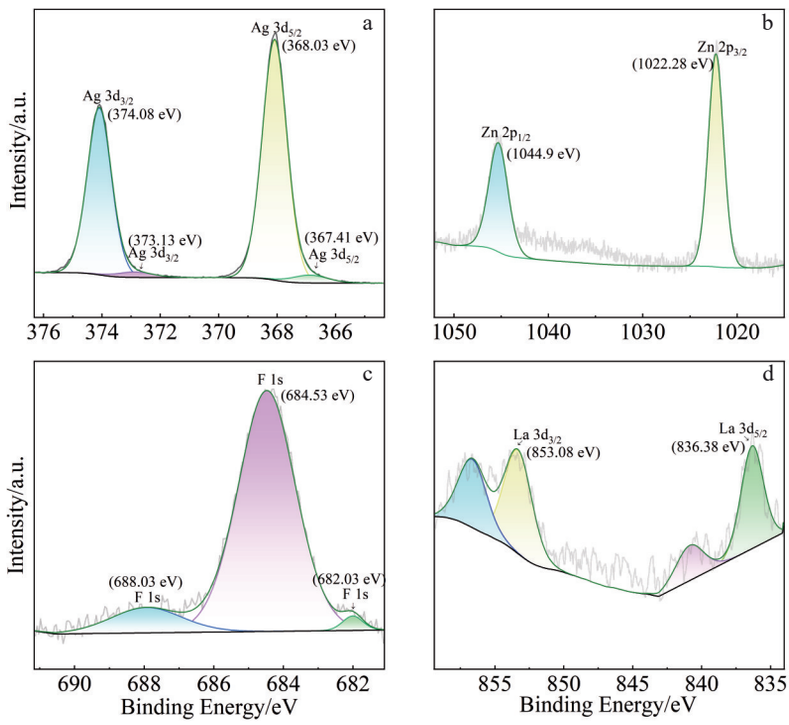


Fig.14 XPS spectra of erosion area of composites in N-C mixture gas: (a) Ag 3d; (b) Zn 2p; (c) F 1s; (d) La 3d

after ionization of the composites, more active metal ions have a stronger ability to attract negative ions in the order of metal activity, and the most active metal element, $La^{3+}$, preferentially combines with $O^{2-}$ and is ionized in $La_2Sn_2O_7$ to form $La_2O_3$. Compared with that in a $CO_2$ atmosphere, the energy emitted by the ion combination is lower in an $N_2$ atmosphere, so the erosion region is smaller. In C-C and N-C mixed atmospheres, c-$C_4F_8$ gas will be ionized into $C^{2+}$ and $F^-$. Because $F^-$ is more electronegative than $O^{2-}$, it preferentially binds to metal ions to form fluoride. The decomposition of c-$C_4F_8$ will produce $CF_x$, which usually occurs at high temperatures[34]. The produced radicals attain dynamic equilibrium. Moreover, $CF_x$ serves as an ideal electrical insulator and thermal conductor, offering excellent chemical

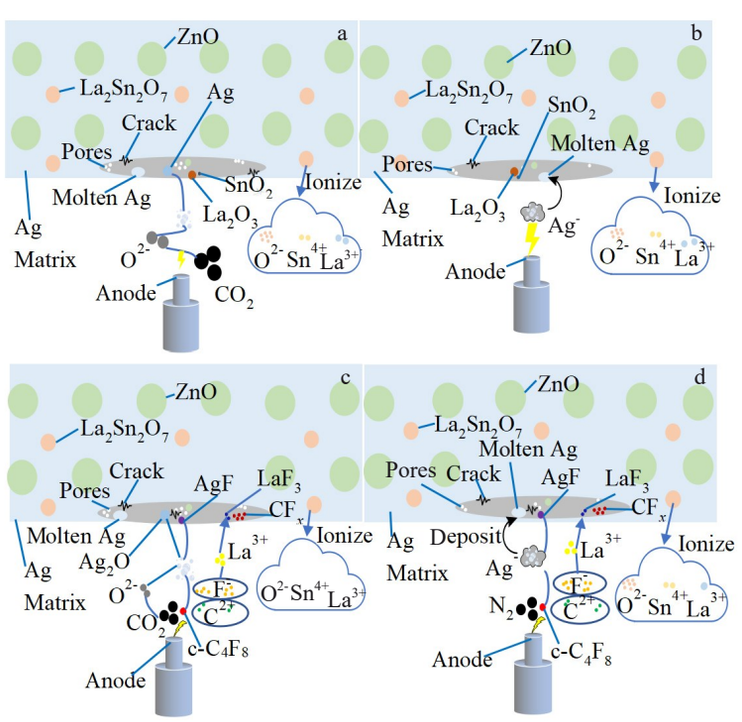


Fig.15 Schematic diagrams of reaction mechanism in different atmospheres: (a) $CO_2$; (b) $N_2$; (c) $CO_2$/c-$C_4F_8$; (d) $N_2$/c-$C_4F_8$

and thermal stability, as well as high thermal conductivity.

## 4 Conclusions

1) The breakdown strength of Ag/ZnO/$La_2Sn_2O_7$ composites increases gradually, and arc energy and arc duration decrease gradually with the increase in c-$C_4F_8$ concentration in both C-C and N-C mixtures. By comparing various arc-erosion parameters, it is found that the addition of a small amount of c-$C_4F_8$ greatly improves the arc-erosion resistance of $CO_2$ and $N_2$. The breakdown strength of the composite material in the C-C-70-30 and N-C-70-30 mixture gases is 203% and 240% of the breakdown strength of the composite material in $CO_2$ and $N_2$, respectively. Compared with the C-C mixture gas, the arc energy in the N-C mixture gas is lower, so the arc volume and erosion area are smaller. The Ag/ZnO/$La_2Sn_2O_7$ composite in an N-C mixture gas shows better arc-erosion performance.

2) There are more pores, spattered particles, and cracks in the composites after arc-erosion in $CO_2$ and $N_2$, and the erosion areas are larger than those in the mixed gases. In the C-C gas mixture, pores, particles, and cracks are also present in the erosion area of the composites after arc-erosion, due to the high $CO_2$ content. The erosion area of the C-C-80-20 gas mixture is relatively small, and particle and pore sizes are clearly reduced. Compared with the C-C mixed gas, the N-C mixture gas only leads to only a few pores in the eroded area. N-C-80-20 mixture gas results in the smallest eroded area and the lowest degree of erosion. The N-C-80-20 mixture gas is considered a better buffer gas for arc-erosion of Ag/ZnO/$La_2Sn_2O_7$ composites.

3) The XPS result reveals that the reaction products in the $N_2$ are $La_2O_3$ and $SnO_2$. Analysis indicates that the reaction products in the $CO_2$ are $Ag_2O$, $La_2O_3$, and $SnO_2$. In mixture gases, $F^-$ will preferentially combine with metal ions to form fluorides, because $F^-$ is more electronegative than $O^{2-}$. Therefore, AgF and $LaF_3$ exist on the surface of the erosion zone. AgF and $CF_x$ are detected in the eroded region of both C-C and N-C mixtures. In addition, an oxidation phenomenon occurs in the C-C mixture, and the reaction product is $Ag_2O$. It shows that the reaction products in the N-C mixed gas are AgF, $CF_x$, and $LaF_3$, and that in the C-C mixed gas are $Ag_2O$, AgF, $CF_x$, and $LaF_3$.

## References


1 Ding J X, Tian W B, Zhang P G *et al. Journal of Advanced Ceramics*[J], 2019, 8(1): 90

2 Li W J, Chen Z Y, Jiang H *et al. Journal of Materials Science & Technology*[J], 2022, 109: 64

3 Guan W M, Liu L L, Zhao L *et al. Rare Metal Materials and Engineering*[J], 2025, 54(6): 1535

4 Qiu Y R, Wang X H, Liang Y *et al. Journal of Alloys and Compounds*[J], 2024, 976: 172966

5 Tao Q Y, Zhou X L, Zhou Y H *et al. Rare Metal Materials and Engineering*[J], 2015, 44(5): 1219

6 Pons F, Cherkaoui M, Ilali I *et al. Journal of Electronic Materials*[J], 2010, 39(4): 456

7 Chen X H, Jia C C, Liu X B. *Rare Metals*[J], 2010, 29(4): 366

8 Hannachi E, Slimani Y, Nawaz M *et al. Journal of Rare Earths*[J], 2023, 41(5): 682

9 Yaykaşlı H, Eskalen H, Kavgacı M *et al. Materials Science and Engineering B*[J], 2026, 323: 118688

10 Zhou J, Jin S Y, Wu R Z *et al. Materials Today Communications*[J], 2025, 48: 113343

11 Wei Z J, Zhang L J, Yang H *et al. Journal of Materials Research*[J], 2016, 31(4): 468

12 Xu C H, Yi D Q, Wu C P *et al. Rare Metal Materials and Engineering*[J], 2010, 39(1): 85

13 Guzmán D, González F, Muranda D *et al. Materials*[J], 2023, 16(10): 3618

14 Xu S H, Chen Z Y, Shao W Z *et al. Journal of Alloys and Compounds*[J], 2024, 1003: 175592

15 Liu F Y, Li T K, Wang R X *et al. Rare Metal Materials and Engineering*[J], 2025, 54(3): 791

16 Wang J, Cao M L, Feng Y e*t al. Canadian Metallurgical Quarterly*[J], 2025: 1

17 Wang J Q, Chang Y Q, Zhu Y C *et al. Materials Research Express*[J], 2021, 8(6): 066528

18 Zhang L J, Shen T, Shen Q H *et al. Rare Metal Materials and Engineering*[J], 2016, 45(7): 1664

19 Cao M L, Feng Y, Wang L L *et al. Journal of Rare Earths*[J], 2022, 40(9): 1488

20 Ding Y, Gao M J, Huang J Q *et al. High Voltage Apparatus*[J], 2025, 61(3): 92

21 Lin L, Chen Q G, Wang X Y *et al. Energies*[J], 2018, 11(12): 3533

22 Zhao H, Feng Y, Zhou Z J *et al. Journal of the European Ceramic Society*[J], 2021, 41(4): 2263

23 Stoller P, Doiron C, Tehlar D *et al. IEEE Transactions on Dielectrics and Electrical Insulation*[J], 2017, 24(5): 2712

24 Xing W J, Zhang G Q, Li K *et al. Proceedings of the CSEE*[J], 2011, 31(7): 119

25 Liu Z H, Feng Y, Jiang N Y *et al. Journal of Electronic Materials*[J], 2023, 52(11): 7818

26 Zhang L C, Xiao D M. *2017 1st International Conference on Electrical Materials and Power Equipment*[C]. Xi'an: Xi'an Jiaotong University, 2017: 521

27 Huang X C, Feng Y, Qian G *et al. Journal of Alloys and Compounds*[J], 2017, 727: 419

28 Mo F, Feng Y, Chen Y Q *et al. Journal of Rare Earths*[J], 2015, 33(3): 327

29 Liu Z H, Feng Y, Yu M *et al. Vacuum*[J], 2024, 219: 112738

30 Zhang M S, Ge F L, Hu H W *et al. International Journal of Thermal Sciences*[J], 2024, 199: 108895

31 Yaws C L. *Matheson Gas Data Book*[M]. Texas: Chemical Industry Press, 2003

32 Gray E W. *IEEE Transactions on Plasma Science*[J], 2007, 33: 151

33 Kim D I, Yim S, Ji S *et al. Small*[J], 2023, 19(41): 2301395
34 Zhang Y, Li Y, Zhang X X *et al. Royal Society Open Science*[J], 2018, 5(10): 181104

# Ag/ZnO/$La_2Sn_2O_7$复合材料在$N_2$、$CO_2$及其与c-$C_4F_8$混合物中的电弧侵蚀行为及机理

包梦婷，郭　轲，姜　云，王炳棠，刘铸汉，凤　仪
（合肥工业大学 材料科学与工程学院，安徽 合肥 230009）

**摘　要：**通过化学共沉淀法合成了$La_2Sn_2O_7$粉末，并通过热压烧结法制备了Ag/ZnO/$La_2Sn_2O_7$复合材料。研究了复合材料在7 kV恒定电压下在$CO_2$、$N_2$、$CO_2$/c-$C_4F_8$和$N_2$/c-$C_4F_8$混合气体中的电弧烧蚀行为和机理。实验结果表明，不同大气压下电弧击穿电流差异非常小，而混合气体中的烧蚀面积、电弧能量和电弧持续时间明显小于$CO_2$和$N_2$。随着c-$C_4F_8$含量的增加，混合气体中的击穿强度逐渐增加，且均高于$CO_2$和$N_2$中的击穿强度。电弧光学图像表明，混合气体中的电弧体积明显小于$CO_2$和$N_2$单一气体中的电弧体积，且随着c-$C_4F_8$含量的增加，电弧体积逐渐减小。烧蚀形貌分析表明，$CO_2$和$N_2$电弧烧蚀后复合材料中存在较多的孔隙、飞溅颗粒和裂纹。在混合气体中，$N_2$/c-$C_4F_8$（80/20）混合气体的烧蚀面积最小，颗粒和孔隙明显减少。在$N_2$/c-$C_4F_8$混合物中观察到的低电弧能量显著降低了电弧体积和烧蚀面积。X射线光电子能谱显示$La_2Sn_2O_7$部分分解为$La_2O_3$和$SnO_2$，而在含有c-$C_4F_8$的混合气体的烧蚀表面上检测出AgF和$CF_x$的存在。

**关键词：**Ag/ZnO/$La_2Sn_2O_7$复合材料；保护气氛；电弧烧蚀行为；烧蚀机理

---

作者简介：包梦婷，女，2001年生，硕士生，合肥工业大学材料科学与工程学院，安徽 合肥 230009，E-mail：1687187907@qq.com